Journal of Quantitative Spectroscopy & Radiative Transfer 224 (2019) 343–354

Contents lists available at ScienceDirect

Journal of Quantitative Spectroscopy & Radiative Transfer

journal homepage: www.elsevier.com/locate/jqsrt

Identification of smoke and polluted clouds based on polarized satellite images

Feifei Xu[a,d], Jinji Ma[a,c,d,*], Shichao Wu[a,c], Zhengqiang Li[b,c]

[a] School of Geography and Tourism, Anhui Normal University, Wuhu 241003, China
[b] Institute of Remote Sensing and Digital Earth, Chinese Academy of Sciences, Beijing 100101, China
[c] Key Laboratory of Optical Calibration and Characterization, Chinese Academy of Sciences, Anhui Province, Hefei 231000, China
[d] Engineering Technology Research Center of Resources Environment and GIS, Anhui Province, Wuhu 241003, China

ARTICLE INFO

Article history:
Received 30 March 2018
Revised 13 November 2018
Accepted 13 November 2018
Available online 16 November 2018

Keywords:
Smoke
Polluted clouds
Detect
Multidirectional polarization

ABSTRACT

Smoke aerosol plays an important role in climate change and the Earth's environment. Using multispectral, multiangle, polarized data for detecting small particles has its unique advantages. In this study, two algorithms were developed to detect smoke aerosols and smoke-polluted clouds (SPC). Multidirectional polarized reflectance (R_p) of different aerosol types was simulated by the UNL-VRTM (Unified Linearized Vector Radiative Transfer Model). Compared to dust, urban, rural and oceanic aerosols, the R_p of smoke at 0.490 μm, 0.670 μm and 0.865 μm increased with the aerosol optical depth (AOD), while other types of aerosols showed the opposite trend. Based on the polarized characteristics of the different aerosol types at three single channels, we found that ratios between polarized reflectances R_p of smoke were more distinct from R_p ratios of other aerosol types for any aerosol optical depth. The polarized reflectance ratios at wavelengths of 0.490 μm, 0.670 μm and 0.865 μm were chosen to detect smoke. We analyzed the radiative characteristics of SPC and smoke-free clouds. In contrast to smoke-free clouds, the simulated total reflectance of SPC increases with wavelength in the spectral range from the visible (VIS) to the near infrared (NIR) by the UNL-VRTM. Additionally, R_p of SPC is enlarged compared to smoke-free clouds in the scattering angle range of 80°-120° at the wavelength 0.865 μm. Therefore, two slopes, the slope of the reflectance in the VIS to NIR spectrum and the slope of the R_p at the scattering angle range from 80° to 120°, were designed to identify polluted clouds.

Finally, the results of the two proposed algorithms were verified in different biomass burning areas by the products of Cloud-Aerosol Lidar with Orthogonal Polarization (CALIOP) and Moderate Resolution Imaging Spectroradiometer (MODIS), demonstrating that smoke and SPC can be well detected. In addition, the proposed algorithm can be applied to a polarized image with channels at 0.490 μm, 0.670 μm and 0.865 μm such as the Chinese Gaofen-5 (or GF-5) satellite.

© 2018 Elsevier Ltd. All rights reserved.

1. Introduction

Every year, a large amount of smoke is released from wildfires into the atmosphere, and this potentially may impact the climate, environment, and air quality [1,2]. Recently, smoke aerosols generated by agricultural biomass burning have caused severe haze episodes. Smoke aerosol contains black and organic carbon which scatter and absorb incoming solar radiation directly [3]. This has a huge negative impact on human health and the ecological environment. The smoke also modifies the shortwave reflection properties of clouds indirectly by acting as a cloud condensation nucleus. In general, smoke aerosols have two impacts on cloud radiative properties, including a cloud albedo effect [4], and a cloud lifetime effect [5].

The clouds that develop in the heavy smoke from biomass burning tend to contain numerous small droplets [6]. Biomass burning produces a high concentration of carbon particles. A large fraction of carbon particles gets attached to sulfate aerosols which later serve as cloud condensation nuclei (CCN) for the formation of cloud droplets. Clouds formed in the smoky air are called smoky pollution clouds or pyro-clouds. The latter is the most extreme form of the smoky pollution cloud, directly feeding on the smoke and the heat from the fires [7].

Since smoke aerosol has a major impact on climate change, the Earth's environment and the properties of clouds, detecting smoke is a very meaningful task. The polarization measurement is sensitive to the fine aerosols and cloud microphysical parameters such

* Corresponding author at: Anhui Normal University, Wuhu 241003, China.
E-mail address: jinjima@ahnu.edu.cn (J. Ma).

https://doi.org/10.1016/j.jqsrt.2018.11.019
0022-4073/© 2018 Elsevier Ltd. All rights reserved.

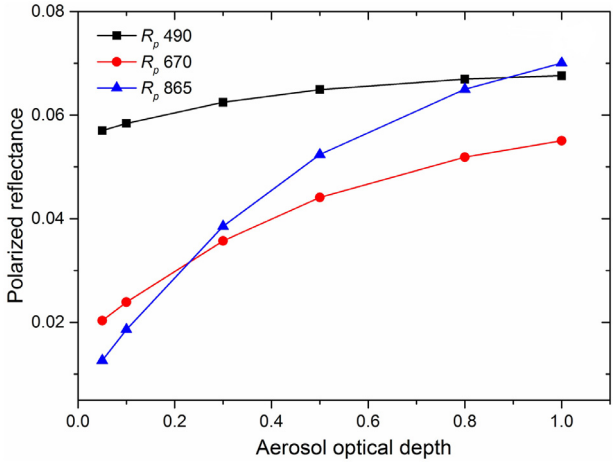

Fig. 1. Polarized reflectance of the smoke simulated at 0.490 μm, 0.670 μm and 0.865 μm. The solar zenith angle is 10°, the relative azimuth is 100° and the view zenith angle is 65°, the surface reflectance is 0.1. The AOD varies from 0.05 to 1.

as the particle size, shape and effective radius [8–11]. The study of clouds and aerosols using a multiwavelength, multiangular polarization has become a very interesting topic recently. Polarization and Anisotropy of Reflectances for Atmospheric Sciences coupled with Observations from a Lidar (PARASOL) is a suitable instrument for this task because of its multidirectional, multispectral, and polarized capabilities [12].

Many researchers have studied smoke by MODIS, SEVIRI (Spinning Enhanced Visible Infrared Imager) and MISR (Multi-angle Imaging SpectroRadiometer) observations. For instance, Xie et al. developed a multi-threshold method to detect smoke plumes with eight MODIS bands [13,14]. Li et al. used a back-propagation neural network to detect fire smoke [15]. Zender et al. characterized a broader variety of physical and optical properties of tropical biomass burning plumes, including shape, optical depth, single-scattering albedo, age, and height [16]. Stachlewska et al. indicated that an increase in the boundary layer top was not only related to an obvious increase in the surface temperature but also to the columnar aerosol optical depth and the surface PM_{10} and $PM_{2.5}$ [17]. After analyzing the global aerosol types retrieved by MISR, Kahn provided a useful aerosol-type quality flag [18]. Some studies show that POLDER (Polarization and Directionality of the Earth's Reflectances) has the ability to monitor biomass burning aerosols. For example, the aerosol index, defined as the Angstrom exponent multiplied by the AOD, makes it possible to link different aerosol types [19]. Goloub et al. found a good correlation between the aerosol index and the ASTER-2 (Advanced Spaceborne Thermal Emission and Reflection Radiometer-2) fire count [20,21]. Tanre et al. used the aerosol index and fire count from ATSR2 (Along Track Scanning Radiometer 2) to roughly identify the aerosol origin [22]. Fan et al. used PARASOL multichannel-polarized data to identify fine aerosols and coarse aerosols [23].

The effects of smoke on the cloud properties, such as cloud albedo, cloud cover and cloud effective radius, have attracted a substantial amount of attention. Martins et al. found high concentrations of low dispersed cloud droplets in biomass burning, while clean conditions revealed an opposite situation [24]. The presence of dense smoke reduces the cloud droplet size from 15 μm to 9 μm. The median liquid-phase cloud droplet radium influenced by biomass burning is 40%–60% smaller than the background clouds [25]. The reflectance of clouds at 0.64 μm drops is from 0.71 to 0.68 with an increase in smoke optical thickness from 0.1 to 2.0 [26]. Smoke also reduces the cloud cover [27,28]. Gautam et al. found a strong positive reflectance gradient in the UV–visible (VIS)-near infrared (NIR) spectrum for clouds embedded in dense smoke, but a negative gradient for clouds free of smoke [29]. However, the identification of pollution clouds is a difficult problem. There are few algorithms to identify smoky pollution clouds. For example, based on the reflectance and the ridge of clouds, Arakawa et al. developed a detective method for ship tracks [30–32]. However, the experiment conditions of this method are strictly limited. Jiang et al., utilized Aura MLS CO and ice water content measurements at 215 hPa to classify ice clouds as "clean" or "polluted" [33,34]. Unfortunately, this method can only handle ice clouds. It is known that the Cloud-Aerosol Lidar and Infrared Pathfinder Satellite Observation (CALIPSO) is an instrument that provides reliable information about the vertical structure of the cloud and aerosol layers, and can be used to distinguish clouds that appear polluted environment. However, the CALIOP has an inherent limitation that cannot perform large-scale simultaneous observations.

In summary, the properties of smoke clouds and smoky pollution clouds have been studied in previous studies, but few algorithms to identify smoke and smoky pollution clouds based on multiangle polarized reflectance. This study developed approaches to detect smoke and SPC by using a PARASOL polarized image. The UNL-VRTM model was used to simulate different aerosol types and SPC. By comparing the R_p of the different aerosol types, we proposed a method based on the ratio of the R_p to identify smoke. By comparing the R_p for pure clouds with SPC, we found that a large R_p value occurred between 80° to 120°, while a small R_p appeared in the primary rainbow peak. SPC tended to show a strong positive reflectance gradient in the VIS-NIR spectrum. These features can be used to identify SPC. Finally, the algorithm was applied to areas polluted by biomass combustion, and the recognition results were compared with the observations of CALIPSO and MODIS. The experimental results showed that the algorithm effectively identified smoke and smoky pollution clouds.

2. Data and methods

2.1. The PARASOL data

PARASOL (Polarization and Anisotropy of Reflectances for Atmospheric Sciences coupled with Observations from a Lidar), launched in December 2004, as an important component of the A-Train, and provides the multispectral (0.443–1.020 μm), multiple directional (up to 16 directions), and polarization characteristics of the solar radiation reflected by the Earth/atmosphere system [12]. Three bands (0.490 μm, 0.670 μm and 0.865 μm) were used to measure the polarization of the reflected solar radiation. In the POLDER level-1 product, three elements of Stokes parameter (I, Q, U) were given.

In this study, the normalized total reflectance R and the polarized reflectance R_p are defined as follows:

$$R = \frac{\pi I}{E_s \cos\theta_s} \tag{1}$$

$$R_p = \frac{\pi\sqrt{Q^2+U^2}}{E_s \cos\theta_s} \tag{2}$$

where I is the radiance, $\sqrt{Q^2+U^2}$ is the polarized radiance, E_s is the top of atmosphere (TOA) solar irradiance, and $\cos\theta_s$ is the cosine of the solar zenith angle.

2.2. The aerosol and cloud model

2.2.1. The aerosol model

Atmosphere aerosols are classified as desert dust (DD), biomass burning (BB), rural and urban [35]. DD is assumed to be mostly

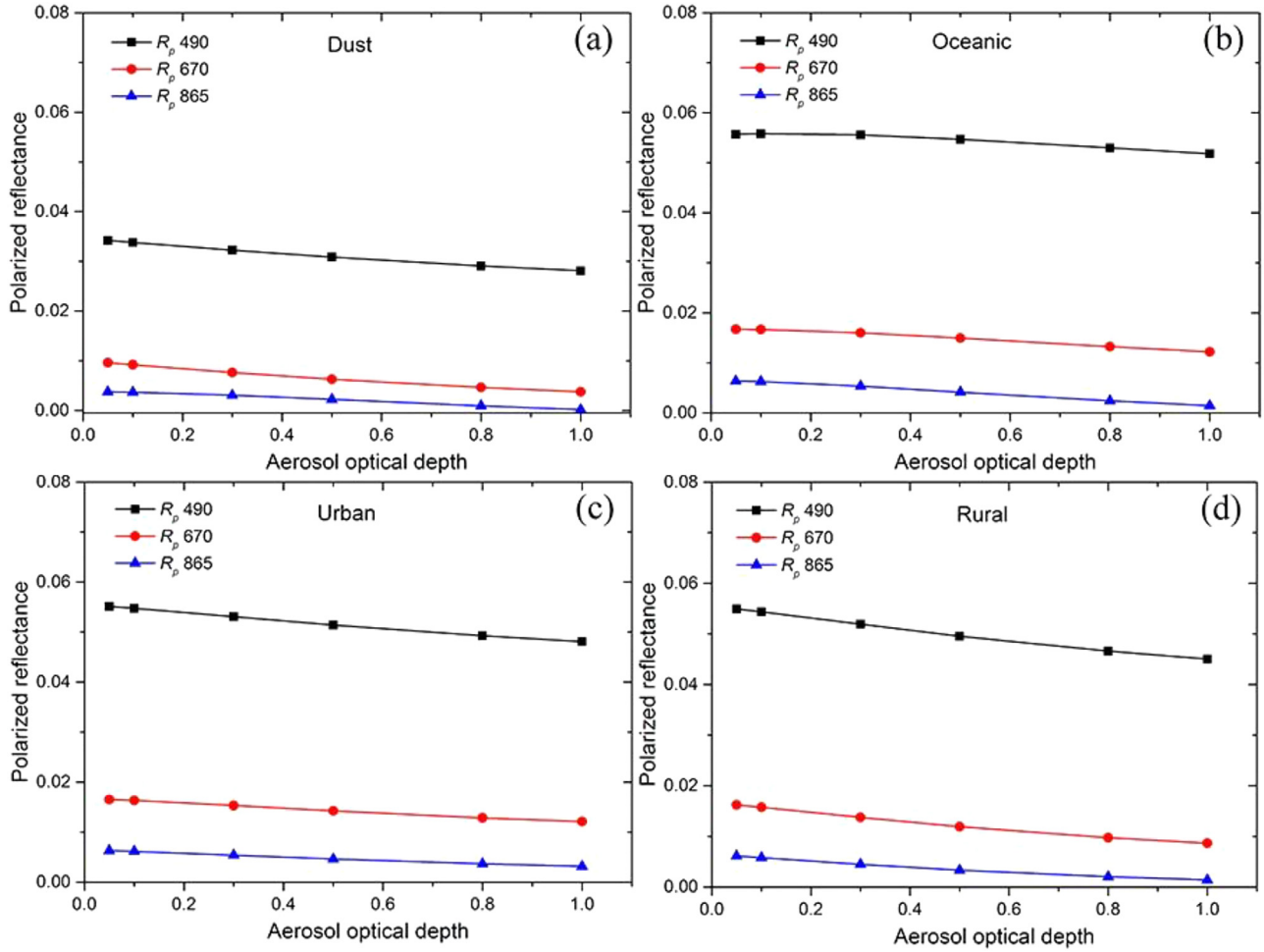

Fig. 2. Polarized reflectance for the other aerosols calculated at 0.490 µm, 0.670 µm and 0.865 µm. (a) Dust, (b) Oceanic, (c) Urban, (d) Rural. The solar zenith angle is 10°, the relative azimuth is 100° and the view zenith angle is 65°. The surface reflectance is 0.1. The AOD varies from 0.05 to 1.

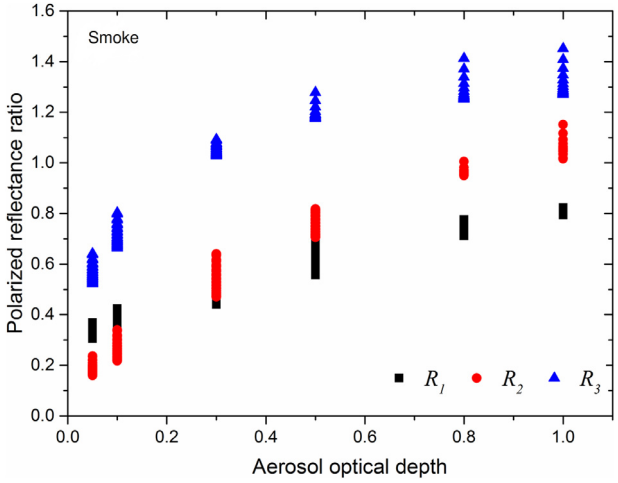

Fig. 3. Polarized reflectance ratios for smoke. The solar zenith angle is 10°, the relative azimuth is 100° and the view zenith angle varies from 60° to 75° in the steps of 5°. The surface reflectance is 0.1. The AOD varies from 0.05 to 1.

mineral soil. BB consists primarily of soot and origin carbon. Rural aerosol is considered as a clean continental aerosol while urban aerosol is considered as a polluted continental aerosol. Oceanic aerosol represents a water-soluble type [36].

Table 1
The size distribution parameters of the different aerosol types.

Aerosol types	$r_f(\mu m)$	σ_f	$r_c(\mu m)$	σ_c
Smoke	0.074	1.68		
Dust	0.5	2.985		
Rural	0.15 ± 0.02	0.54 ± 0.06	2.74 ± 0.36	0.75 ± 0.04
Urban	0.18 ± 0.09	0.52 ± 0.07	3.25 ± 0.43	0.65 ± 0.06
Oceanic	0.3	2.51		

In generally, a bimodal lognormal distribution well describes aerosol [37], which is defined as

$$\frac{dV}{d\ln r} = \frac{V_f}{\sqrt{2\pi}\ln\sigma_f} e^{-\frac{(\ln r - \ln r_f)}{2\ln^2\sigma_f}} + \frac{V_c}{\sqrt{2\pi}\ln\sigma_c} e^{-\frac{(\ln r - \ln r_C)}{2\ln^2\sigma_c}} \quad (3)$$

where the parameters V_f, r_f and σ_f are the total volume concentration, the geometric mean diameter, and geometric standard deviation of the fine mode particles, respectively. The corresponding parameters V_c, r_c and σ_c stand for coarse mode particles. Tables 1 and 2 show the average size and complex refractive index of the different aerosol types. The complex refractive index of smoke (Table 2) is from Dubovik et al. [38,39]. The size distribution parameters and the complex refractive index of urban, rural and oceanic aerosols are from Hao et al. [40]. In our simulations, smoke, urban, rural and oceanic aerosols are assumed to be spherical particles. The optical properties of those aerosols were calculated by the Mie theory. However, the scattering properties of the

Table 2
Complex refractive index of the aerosol types at different wavelengths.

Aerosol types	0.490(μm)		0.670(μm)		0.865(μm)	
	n_r	n_i	n_r	n_i	n_r	n_i
Smoke	1.55	0.01945	1.55	0.0185	1.55	0.0175
Dust	1.53	0.008	1.53	0.008	1.52	0.008
Rural	1.58	0.008	1.60	0.007	1.62	0.010
Urban	1.46	0.014	1.48	0.010	1.50	0.011
Oceanic	1.382	6.41E−9	1.376	5.04E−3	1.372	1.09E−6

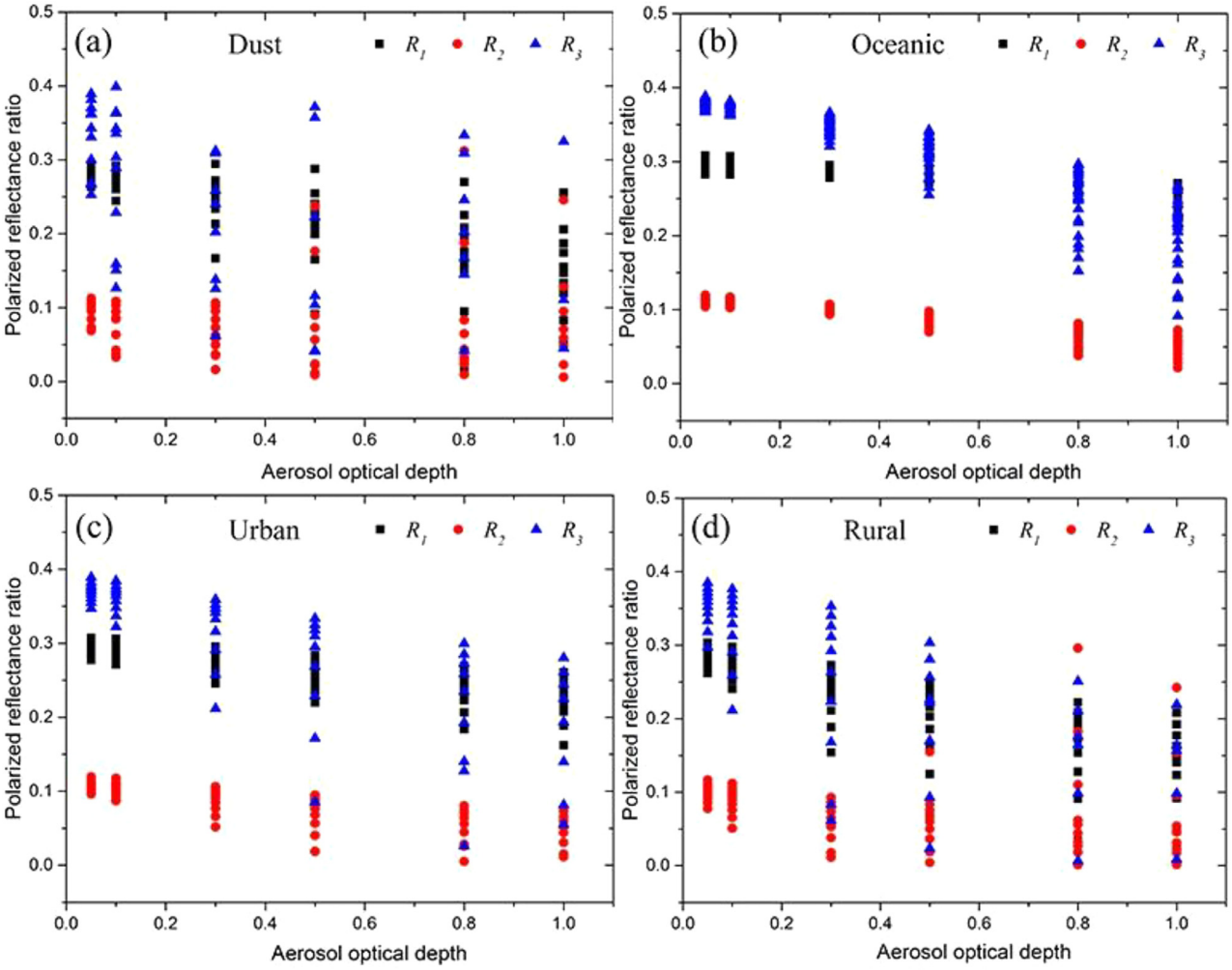

Fig. 4. The polarized reflectance ratios for other aerosols; (a) Dust, (b) Marine, (c) Urban, (d) Rural. The solar zenith angle is 10°, the relative azimuth is 100° and the view zenith angle varies from 60° to 75° in the steps of 5°. The surface reflectance is 0.1. The AOD varies from 0.05 to 1.

dust particles were calculated by the T-matrix, since they are assumed to be non-spherical particles.

2.2.2. The liquid cloud model

The Hansen-Gamma size distribution is usually used to describe water clouds [41], which can be defined as

$$n(r) = \mathrm{C}r^{\alpha}e^{-\beta r^{\gamma}} \tag{4}$$

$$\mathrm{C} = \frac{\gamma \beta^{\frac{\alpha+1}{\gamma}}}{\Gamma\left(\frac{\alpha+1}{\gamma}\right)},\ \gamma = 1 \tag{5}$$

$$\alpha = \frac{1-3V_{eff}}{V_{eff}},\ \beta = \frac{1}{R_{eff}V_{eff}} \tag{6}$$

where R_{eff} and V_{eff} are the effective radius and the effective variance, respectively. In this study, a liquid water droplet model, with an effective radius of 10.0 μm and effective variance of 0.1, was considered. The scattering properties of the water cloud particles were calculated by the Mie theory.

2.3. Methods

2.3.1. An algorithm to identify smoke

To compare the differences of the R_p values between smoke and other aerosol types (dust, oceanic, urban, rural), the UNL-VRTM was utilized. The UNL-VRTM was designed by Wang et al. [42], which comprises the VLIDORT [43] for radiative transfer. The UNL-VRTM is a model redeveloped on the basis of VLIDORT, which retains most of the content of the VLIDORT model.

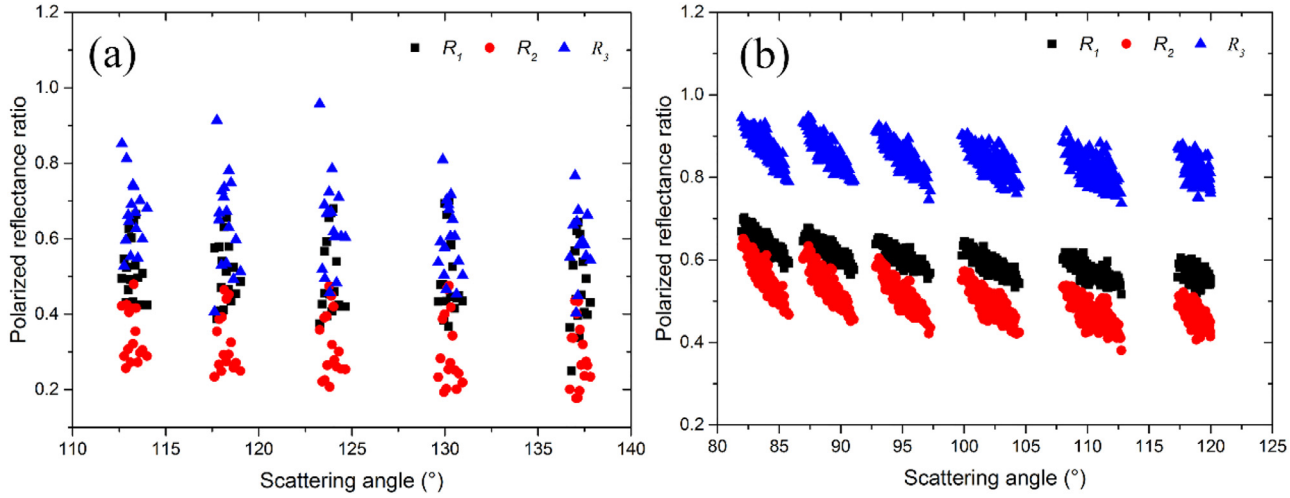

Fig. 5. Polarized reflectance ratios derived from the PARASOL data, (a) smoke over the African continent on August 12, 2006; (b) smoke over Victoria on December 18, 2006.

A realistic scenario of the solar zenith angle and the view zenith angle for PARASOL were at 0°–75°. Generally, the PARASOL scattering angles usually ranges from 70° to 160° for PARASOL observation geometry. The polarized reflectance is insensitive to smoke over a large scattering angle [44], and thus, we narrowed down to the scattering angle to a range of 80°–120°. The scattering angle was be defined as $\cos\Theta = \cos\theta_s cos\theta_v + \sin\theta_s sin\theta_v \cos(\varphi_s - \varphi_v)$, where, θ_s and θ_v are the solar zenith angle and the viewing zenith angle, respectively. φ_s and φ_v are the solar azimuth angle and the viewing azimuth angle, respectively.

In this simulation, the solar zenith angle was 10°, the relative azimuth was 100° and the view zenith angle varied from 60° to 75° in the steps of 5°. Thus, the scattering angle was at range from 103° to 120°. The surface reflectance was fixed at 0.1, and the optical thickness varied from 0.05 to 1.0. Figs. 1 and 2 only show the results of the simulated conditions with a solar zenith angle of 10°, a relative azimuth angle of 100°, and a view zenith angle of 65°.

Fig. 1 shows that the R_p of smoke increases greatly as the AOD increases at wavelengths of 0.490 μm, 0.670 μm and 0.865 μm. Fig. 2 indicates the R_p values of dust, oceanic, urban, and rural aerosols as a function of the AOD. Comparing the upper two figures (Figs. 1 and 2), there was an obvious difference. The R_p of the other aerosol types decreased as the AOD increased at 0.490 μm, 0.670 μm and 0.865 μm. This property may be an important feature to identify smoke.

From the above obvious characteristics, the smoke aerosol was distinguished from the other aerosol types based on the polarization measurement. However, from the above two figures, it was not easy to accurately identify smoke aerosol only by the polarization reflectance thresholds of the three polarization bands in the different aerosol optical depths (AODs). Based on the above polarized characteristics, we tried to use the polarized reflectance ratio test to identify smoke aerosol based on three polarized channels. One major advantage of the polarized reflectance ratio is to reduce the dependence on the radiometer calibration and the incoming flux [45]. First, the spectral ratios of the R_p values among 0.490 μm, 0.670 μm and 0.865 μm were defined as:

$$R_1 = R_p670/R_p490 \tag{7}$$

$$R_2 = R_p865/R_p490 \tag{8}$$

$$R_3 = R_p865/R_p670 \tag{9}$$

where, R_p490, R_p670 and R_p865 represent the polarized reflectances at 0.490 μm, 0.670 μm and 0.865 μm, respectively.

The R_p of smoke has small values at large side scattering angles. Since the polarized reflectance of smoke was insensitive to changes in the AOD over a wide range of scattering angles, the R_p at scattering angles narrowed down to 80°–120° was selected. The polarized reflectance of the smoke, dust, ocean, urban, and rural aerosols was obtained from the above simulation. Then, we calculated the polarized reflectance ratios (R_1, R_2 and R_3).

Fig. 3 shows the polarized reflectance ratios (R_1, R_2, R_3) for smoke at a solar zenith angle of 10°, a relative azimuth of 100°, a view zenith angle varies from 60° to 75° in the steps of 5°, a surface reflectance of 0.1, and an AOD that ranged from 0.05 to 1.0. By plotting the spectral ratios of the polarized reflectance changes with the AODs (Fig. 3) at a scattering angle that ranged from 80° to 120°, an obvious up trend against the AODs was seen. For all smoke, the R_1, R_2 and R_3 increased with the AOD, with minimum that appeared at a small AOD. For a heavy smoke plume with a larger AOD, the ratios tended to be stable. The R_1 positively correlated with the optical thickness. It was in the range of 0.3–1.0. The R_2 increased with the AOD, which ranged between 0.2 and 1.2. R_1 and R_2 were very close to each other when the AOD was less than 0.6, and both of them were greater than 0.2. The R_3 was greater than 0.4. Compare to R_1, R_2 and R_3, R_3 had the largest value, with a minimum value of 0.4 and a maximum value that stayed at 1.5.

Fig. 4 shows the polarized reflectance ratios for the different aerosol types including dust, marine, urban and rural aerosol. R_1, R_2 and R_3 decreased as the AOD increased for those aerosols. This was the most distinctive feature from smoke. In addition, all the ratios were less than 0.4. For these four types of aerosols, R_1, R_2 and R_3 were usually less 0.3, 0.15 and 0.4, respectively. The analysis above indicated that the polarized ratios identified thick smoke. In fact, it was difficult to detect the pixels with magnitudes that were relatively low. To eliminate the influence of the polarized reflectance of the ground, the value of R_p at 0.865 μm needs to be greater than 0.02 [46].

To verify the rationality of the thresholds, we selected real scenes where biomass burning occurred in Africa on August 12, 2006 and in Victoria on December 18, 2006. The statistical results of the threshold are shown in Fig. 5. Fig. 5a indicates that in smoke-contaminated Africa, the R_1 (black dot) is mainly distributed between 0.4 and 0.7, and the R_2 (red dot) is mainly in the range of 0.2–0.5. The R_3 (blue dot) was focused on 0.4–1.0. Fig. 5b indicates the statistical thresholds in Victoria. The thresholds from

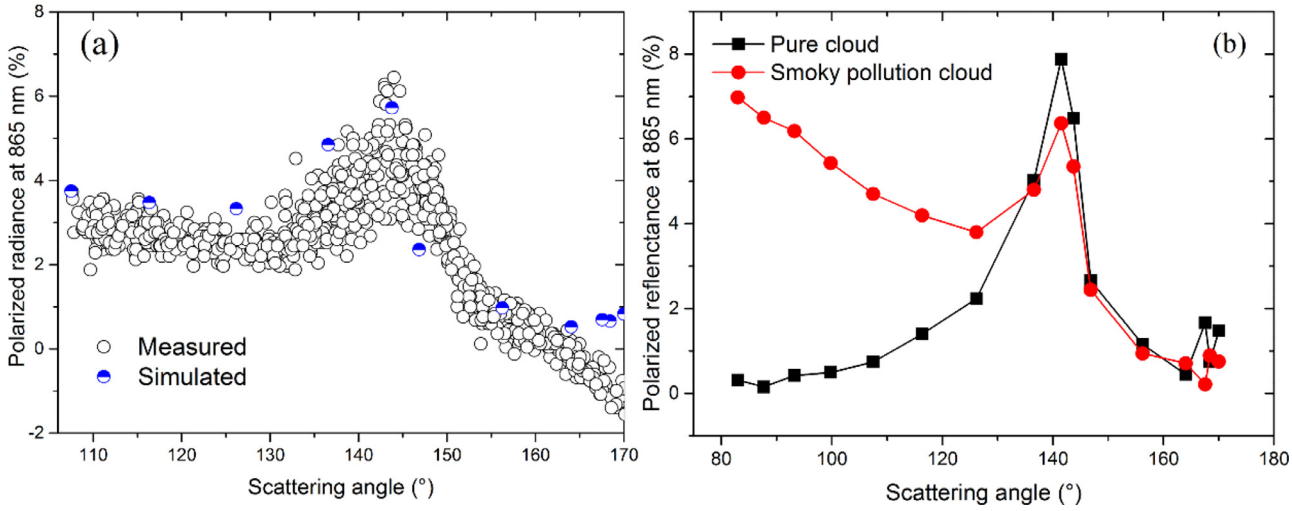

Fig. 6. (a) Comparison of the simulation and measured data from PARASOL for pollution clouds. The PARASOL measured data was from Liuzhou, China on April 3, 2006. The simulated data total optical thickness was 1. (b) The polarized reflectance of water cloud and smoky pollution cloud was simulated at 0.865 μm. The cloud optical thickness was 5.

Table 3
The threshold tests and threshold ranges used for detecting smoke.

Threshold test	Threshold range
R_1	0.3–1.0
R_2	0.2–1.2
R_3	0.4–1.5
R_p865	0.02

the theoretical calculation were consistent with the statistical results.

The polarized reflectance ratio was used to detect the smoke plume over land. The method was as follows: the scattering angle range was from 80° to 120°; R_1 was greater than 0.3 and was less than 1.0; R_2 was greater than 0.2 and was less than 1.2; and R_3 was greater than 0.4 and was less than 1.5. In addition, the R_p at 0.865 μm was greater than 0.02. The threshold tests and ranges are shown in Table 3.

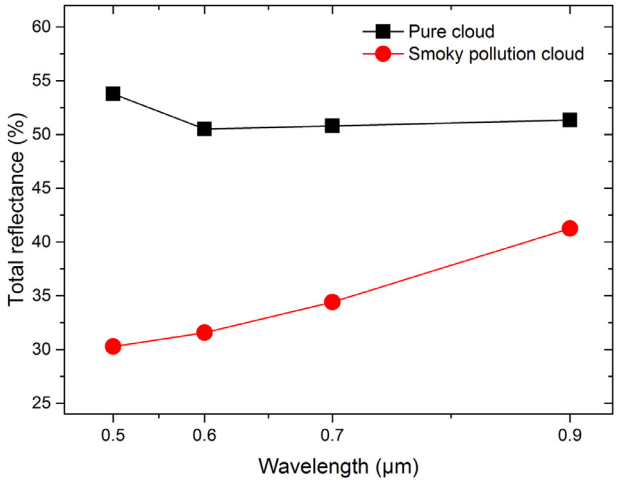

Fig. 7. The spectral reflectance of the clean cloud and smoky pollution cloud.

2.3.2. An algorithm to identify smoky pollution clouds

Two scenarios that include pure clouds and smoky pollution clouds at the wavelength of 0.865 μm were considered in the model. In our radiative transfer calculations, the solar zenith angle was 57°. In pure clouds scenarios, a single-layer cloud was assumed to have an optical thickness of 3 and a height of 1–2 km. To model smoky pollution clouds, our scenarios contained a single-layer model, with a bimodal size distribution, one water cloud model and a smoke particle model. In this study, an effective radius of 10.0 μm and an effective variance of 0.1 for liquid clouds were considered in the model. The smoke aerosol particles were defined as fine modes and assumed spherical particles, and the size parameters are given in Table 1. This case represented an external mixture of cloud droplets and aerosols particles. Fig. 6a represents the comparison of the simulated results and the measured data from PARASOL for pollution clouds contaminated by smoke. The PARASOL measured data was from Liuzhou, China on April 3, 2006. In the simulation, the optical thickness of the water cloud was 1. We concluded that the simulated results were in accordance with the PARASOL observation data (Fig. 6a), which meant that the simulation method was reliable.

The results of the R_p of the pure cloud and smoky pollution cloud at the wavelength of 0.865 μm are shown in Fig. 6b. The cloud optical thickness was 5. Compared to the pure cloud, the R_p of the smoky pollution cloud was enlarged at the wavelength of 0.865 μm and at scattering angle ranges from 80° to 120°. The R_p tended to have a negative slope for the pollution clouds but had a positive slope for pure clouds at scattering angle ranges from 80° to 120°. The smoky pollution clouds contained more small particles which lead to R_p increases at the side scattering angle. The additional polarized signals corresponded to the R_p generated by the aerosols.

The R_p was usually greater than 0.02 for the smoky pollution cloud, while it was less than 0.02 for the pure cloud at scattering angle ranges from 80° to 120°. In addition, a polarized reflectance attenuation appeared around scattering angle of 140° (rainbow region). According to the theory of radiative transfer, the R_p is mainly caused by single scattering rather than multiple scattering. The smoky pollution clouds, which contains many small particles, hold more multiple scattering than single scattering [47]. Therefore, the polluted cloud had a lower R_p in the rainbow region.

Fig. 7 shows the spectral reflectance of the pure clouds and smoky pollution clouds in the visible to near infrared spectrum, as calculated by the UNL-VRTM model with a surface albedo of 0.05. The smoky pollution clouds tended to a lower reflectance

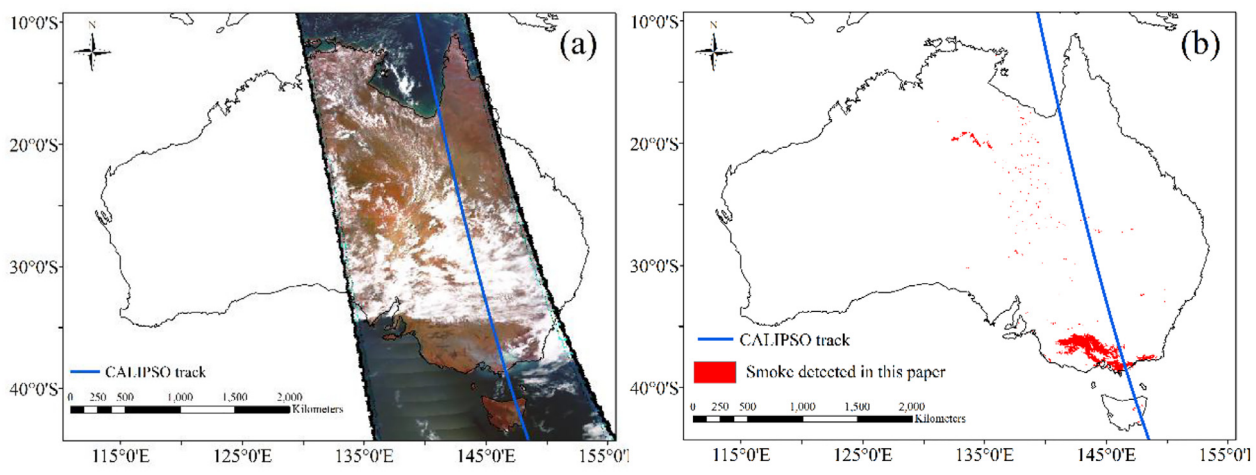

Fig. 8. (a) True color PARASOL RGB composite over Australia on December 20, 2006 relative to 04-07-49 UTC, (b) the results of the smoke detected by the proposed method. The blue solid line represents the CALIPSO orbit track, the red feature indicates the smoke detected.

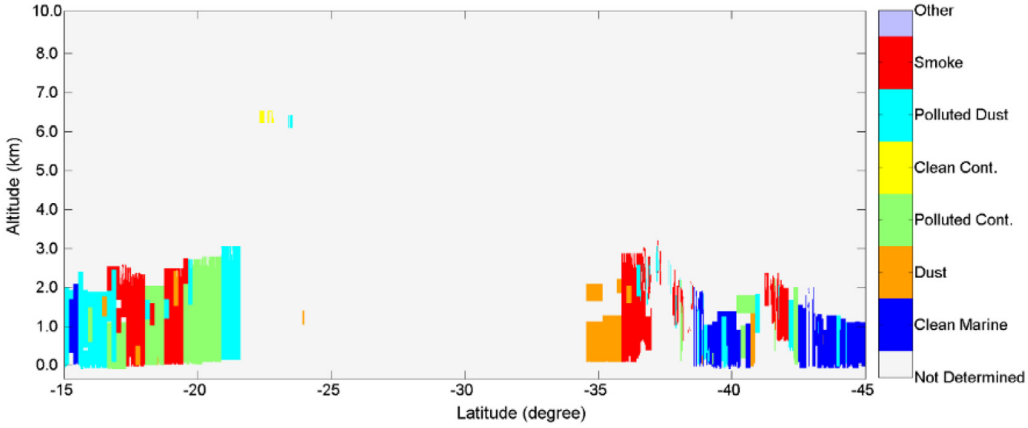

Fig. 9. Different aerosol types derived from the CALIOP measurements as a function of latitude.

value due to the suppression in the visible spectrum. A strong positive reflectance gradient appeared in the visible to near infrared spectrum for the clouds polluted by smoke, but a flat spectrum was seen for the smoke-free clouds. The clouds in the presence of smoke appeared darker, and the absorption was enhanced at shorter wavelengths, resulting in a lower reflectance in the visible spectrum. This was also consistent with the result by Gautam [29].

Based on the analysis above, three features were used to identify smoky pollution clouds. First, the R_p was greater than 0.02 for the smoky pollution cloud at scattering angle ranges from 80° to 120° at the wavelength of 0.865 μm (Eq. 10). Second, there was a negative linear fitting value for R_p at scattering angle ranges from 80° to 120° in the wavelength of 0.865 μm (Eq. 11). Additionally, there was a positive slope for the total reflectance in the 0.490 μm to 0.865 μm spectrum for the clouds embedded in smoke (Eq. 12). Therefore, we designed two slope tests to identify smoky pollution clouds. The two slope tests are described as:

$$R_p^{[80^\circ,\ 120^\circ]} > 0.02 \tag{10}$$

$$slopeR_p^{[80^\circ,120^\circ]} < 0 \tag{11}$$

$$slopeR^{[0.490-0.865]} > 0 \tag{12}$$

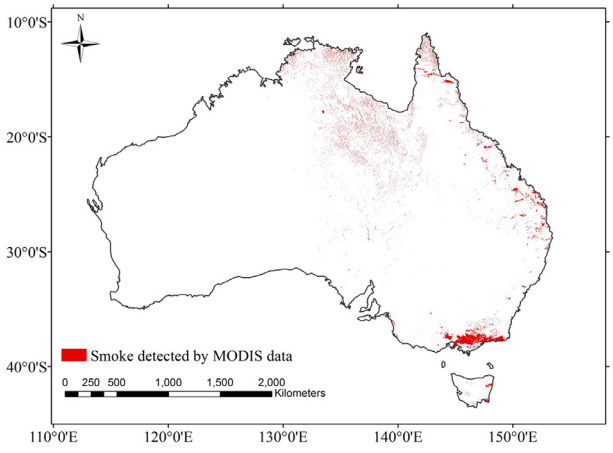

Fig. 10. The results of the smoke aerosol detected by the Aqua MODIS data with a multi-threshold method on December 20, 2006.

where, $R_p^{[80^\circ,\ 120^\circ]}$ represents the R_p at scattering angle ranges from 80° to 120°. The $slopeR_p^{[80^\circ,120^\circ]}$ is the slope for R_p at scattering angle ranges from 80° to 120°, and $slopeR^{[0.490-0.865]}$ is the slope of the total reflectance at wavelengths ranging 0.490 μm–0.865 μm.

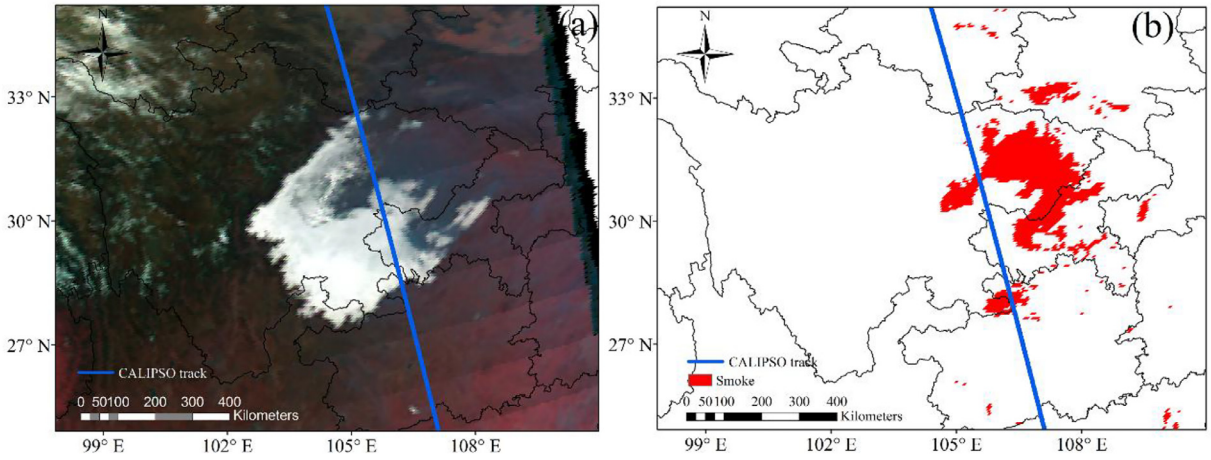

Fig. 11. (a) True color PARASOL RGB composite over China on December 9, 2008 UTC 05-49-51 (b) the results of the smoke detected by our algorithm.

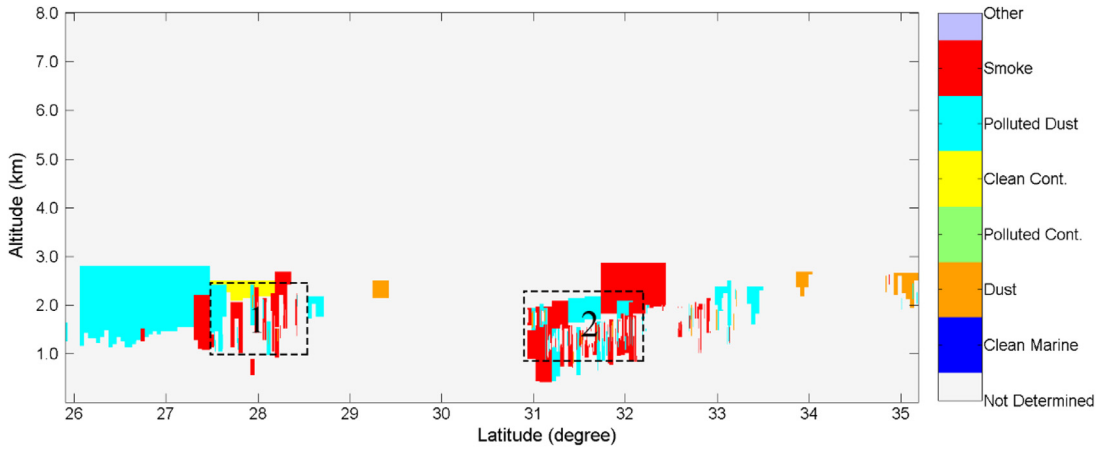

Fig. 12. Aerosol types derived from the CALIOP measurements as a function of latitude.

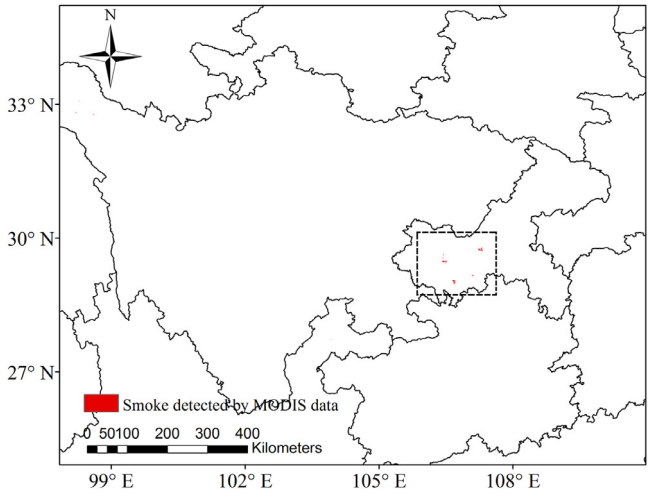

Fig. 13. The results of smoke aerosol on December 9, 2008 UTC 06–20, as detected by the Aqua MODIS data, with a multi-threshold method, as developed by *Xie* [13,14].

3. Application and discussion

Here, we verified the two proposed algorithms by applying them under different smoke-affected cases. The Cloud-Aerosol Lidar with Orthogonal Polarization (CALIOP) onboard NASA's Cloud-Aerosol Lidar and Infrared Pathfinder Satellite Observations (CALIPSO) was launched in April 2006 [48]. As part of the A-train constellation, PARASOL and CALIPSO satellites observe the same scene within 1–2 min. The CALIPSO level 2 vertical feature mask product, which describes the vertical and horizontal distribution of the cloud and aerosol types [47,48], was furtherly used to affirm the effectiveness of the proposed algorithm. The flight orbit of MODIS has the same coverage area as PARASOL but is 1 min and 15 s behind. The MODIS data also verified the reliability of the smoke detection algorithms.

For the PARASOL level 1B data, the first step is cloud detection. The POLDER cloud pixels detection was developed by Bréon and Colzy [49]. There are cloud pixel mistakes without considering the underlying snow or ice surface and the change of time and space, and the threshold in the algorithm is fixed. To identify the cloud pixel accurately, a new cloud detection algorithm, with a dynamic threshold that changed with the different atmospheric models, was adopted [50]. In addition, ice and snow cover were considered in this new algorithm.

3.1. Application of the smoke detection algorithm

3.1.1. Biomass burning in Australia

Large scale of forest fires occurred in Australia in December 2006. In Fig. 8, the PARASOL RGB composite over Australia shows an episode of biomass burning plumes over Victoria on December 20, 2006. The CALIOP orbit track is illustrated with a blue line in Fig. 8. Fig. 8b shows the results of the smoke detection. A small

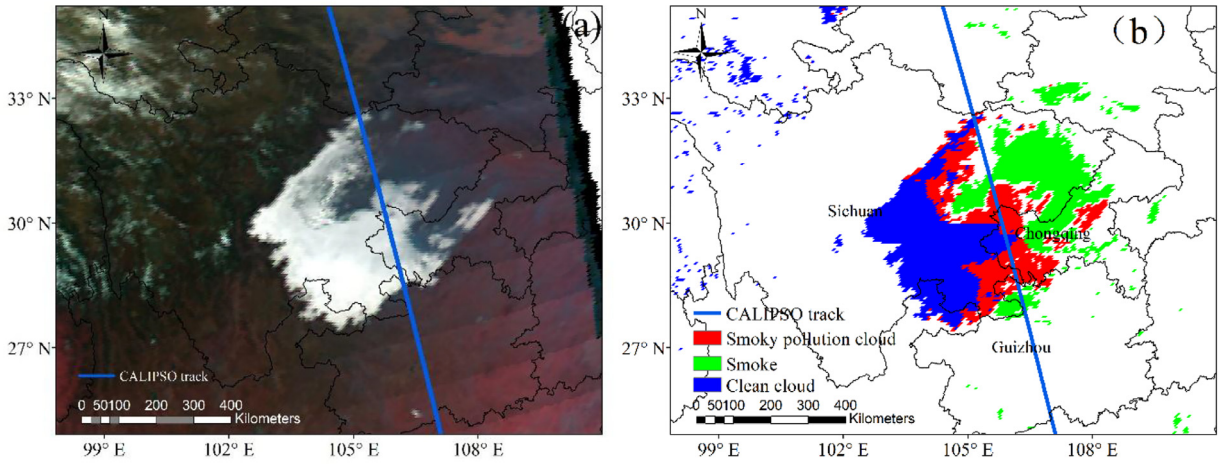

Fig. 14. The results of the pollution clouds in Sichuan, China on December 9, 2008, as detected by the proposed method. (a) True color POLDER RGB composite, (b) the results of the smoky pollution cloud (red color) and clean cloud (blue color) detected by our algorithm. The blue solid line represents the CALIPSO orbit track, the red feature indicates the smoky pollution cloud, the green feature indicates the smoke detected, and the blue feature (no blue solid line) indicates the cloud-free region.

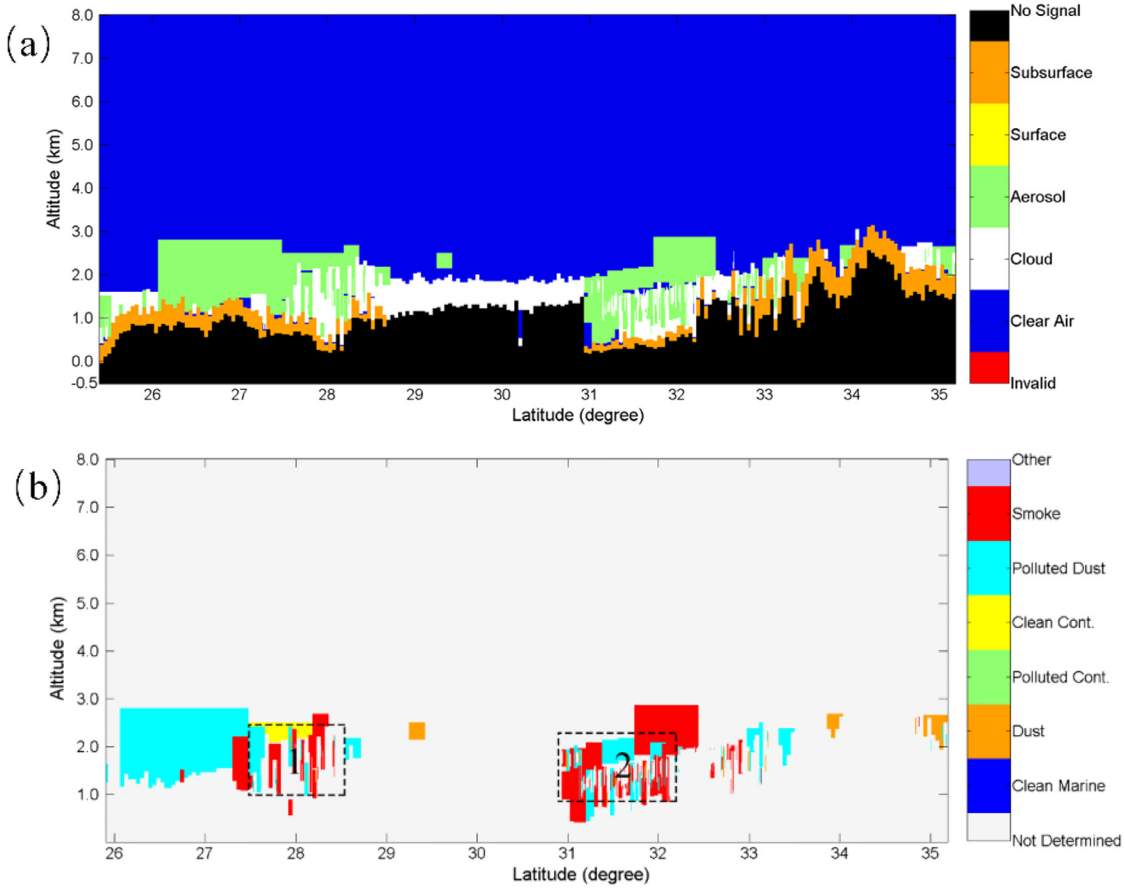

Fig. 15. (a) All feature types and (b) aerosol types derived from the CALIOP measurements on December 9, 2008 as a function of latitude.

amount of smoke was distributed in the center of Australia, while a large amount of smoke was concentrated in Victoria near the forest fire sources. Compared to the true color images (Fig. 8a), most of the smoke plumes were detected.

For evaluating the effectiveness of our algorithms, CALIPSO Level 2 vertical feature mask products are used, which provide the altitude and aerosol types. Fig. 9 shows the corresponding aerosol types. Our algorithm detected a large amount of smoke excites at latitudes of 37°S and 42°S, with an altitude of 1–2 km. However, CALIPSO fails to distinguish the aerosol types due to the presence of the thick clouds between latitudes 23° S and 34° S [51].

While CALIPSO has limited spatial sampling and only provides observations along the ground track, MODIS provides a large scale of observations that are multispectral, which can be used to verify the smoke results for a large area. The smoke was detected using the multi-threshold method development by *Xie* [13,14] for MODIS data. The results of the multi-threshold method application to the Aqua MODIS data on the same day at approximately 04:25 UTC

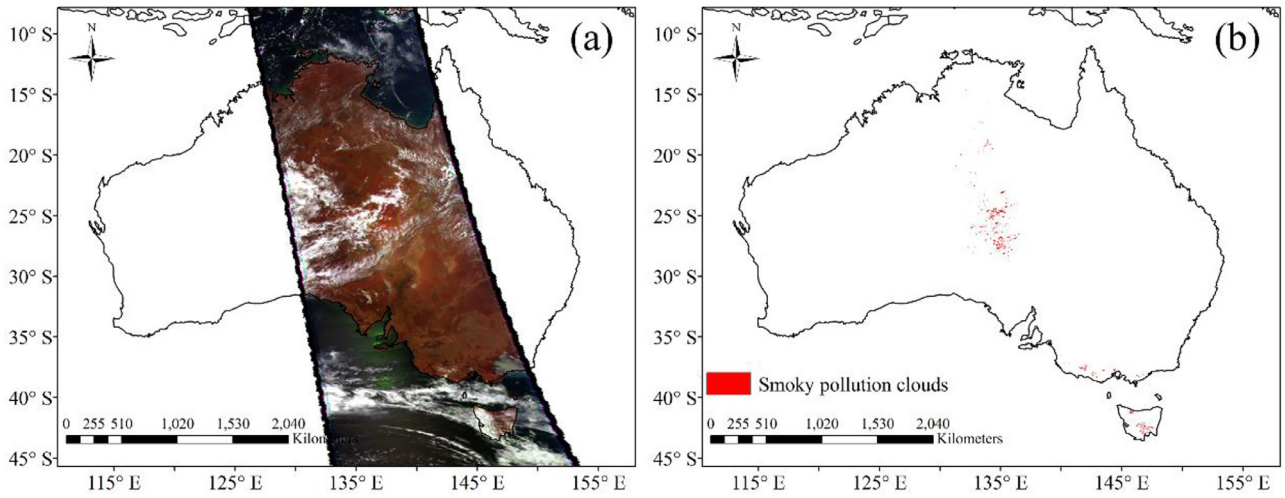

Fig. 16. (a) PARASOL RGB composites relative to the December 18, 2006 UTC 04-20-10 measurement in total radiance, (b) the distribution of the smoky pollution clouds identified by our algorithm.

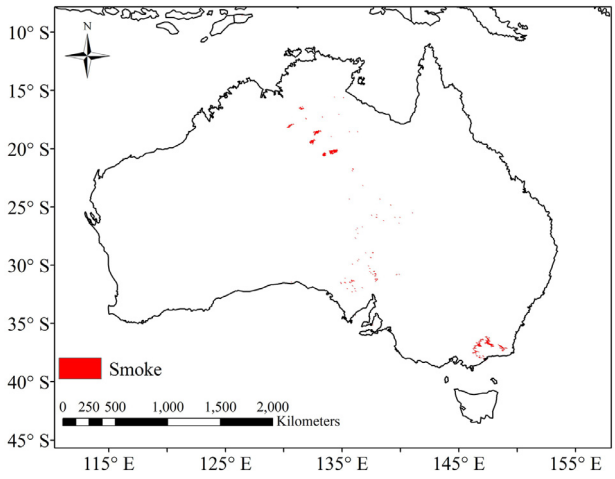

Fig. 17. The distribution of the smoke detected by our algorithm from the PARASOL image relative to December 18, 2006 UTC 04-20-10, which is the same time as Fig. 16.

are shown in Fig. 10 and indicate that heavy smoke plumes were well captured in Victoria. Compared to Fig. 8b, the results indicate that the proposed algorithms detected heavy smoke plumes well, but they still had difficulty in separating the light smoke plumes. For example, as Fig. 8b shows, smoke is detected around latitudes 20° S, 37° S and 42° S by our algorithm. In addition, the MODIS detected a substantial amount smoke at the same latitude (Fig. 10). This suggests that our algorithm effectively identified smoke.

3.1.2. Smoke plumes over China

Smoke plumes caused by major wildfires in China on December 9, 2008 posed a severe threat to the local air quality and the public health. As shown in Fig. 11a, it is obvious that the smoke mainly covered Sichuan around the water clouds in the PARASOL RGB map. The CALIOP orbit track is illustrated with the blue line in Fig. 11.

The smoke results detected by our algorithm are shown in Fig. 11b with a red color. A lot of smoke was seen in Sichuan by the residents due to the biomass burning. We first validated the smoke results by CALIOP measurements. Fig. 12 shows a large amount of smoke covering latitudes 28°N (black box 1) and 31°N–32°N (black box 2). In Fig. 11b, smoke is also detected at the same latitude at the same time. Thus, the results of the proposed algorithm were consistent with CALIPSO observations. Fig. 13 represents the distribution of smoke on the same day, as detected by MODIS with a multi-threshold method. The main smoke is in the dotted line frame (Fig. 13). Compared to Fig. 11a, a large amount of smoke is not detected in Fig. 13. The algorithms development by *Xie* [13,14] were not able to detect smoke in this area. However, our algorithm effectively detect smoke in this area.

3.2. Application of smoky pollution cloud detection algorithm

Next, we applied the proposed smoky pollution clouds algorithm in Sichuan, China on December 9, 2008. As shown in Fig. 14a, it was obvious that smoke was mainly covered in Sichuan around clouds in the PARASOL true color image (RGB map). The CALIOP orbit track was illustrated with the blue line in Fig. 14. We verified the effectiveness of the algorithm by comparing our results with the aerosol types derived from the CALIPSO and smoke results detected by the PARASOL. Smoky pollution clouds usually occur in an area with large numbers of smoke plumes. If water clouds were embedded in the smoke environment, we defined the clouds as polluted clouds [4]. Fig. 14b shows the results of smoky pollution clouds on December 9, 2008. The pollution clouds were mainly concentrated near the smoke pollution. Fig. 14b shows the results of smoky pollution clouds were mainly distributed at the latitudes of 28°N, 31°N and 33°N. The location of the clean clouds was away from smoke, while smoky pollution clouds usually occurred in the area with large numbers of smoke plumes.

The vertical distribution of clouds and aerosols derived from CALIPSO showed in Fig. 15a and b. Here, the clouds were focused on the latitudes of 28°N, 31°N and 33°N (box 1 and box 2). Water cloud and smoke aerosol were distributed at altitudes of 1 km–2 km. And most of clouds were embedded in smoke environment. Meanwhile, the results of smoky pollution clouds indicated clouds polluted by smoke. In addition, the clouds at the junction of clouds and aerosols were detected as polluted clouds, it proved the correctness of the algorithm. All in all, the above results indicated that the proposed algorithm had a good performance for detecting polluted clouds over biomass burning contaminated areas.

Here, we focused on another day over Australia. Fig. 16a shows the true RGB of the PARASOL on December 18, 2006 in Australia. There was only small cloud coverage in the mainland. Fig. 16b shows that the polluted clouds are mainly distributed in the latitudes of 20°S, 30°S, and 37°S. Fig. 17 represents the results of the smoke detected by the polarized reflectance ratio method. These were the same times and areas as in Fig. 16. The smoke was dis-

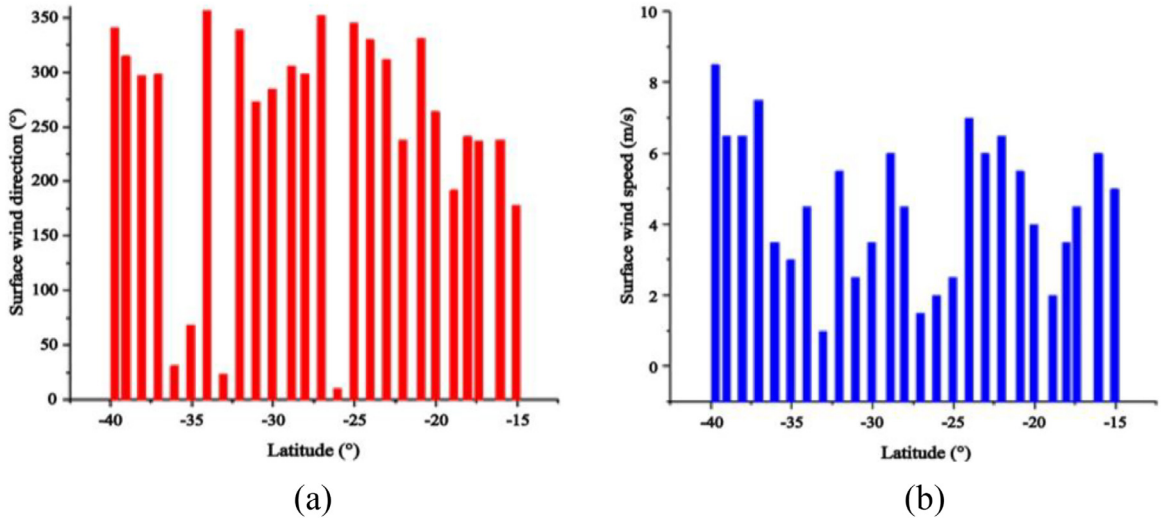

Fig. 18. Surface wind direction (a) and surface wind speed (b) both derived from the PARASOL RB2 products relative to December 18, 2006 in Australia.

tributed at latitudes 20°S, 30°S and 37°S. This showed that the distribution of the smoky pollution clouds (Fig. 17) was always consistent with that of smoke aerosol. Note that, in the south east, the smoke appeared to be in a much more eastern position relative to the smoky pollution clouds. In this case, we considered the wind speed and wind directions at the local area. The PARASOL radiative budget level 2 (RB2) products provided the parameters of the surface wind direction (°) and the surface wind speed (m/s), which derived were from ECMWF (European Centre for Medium-Range Weather Forecasts). The RB2 products were given at a spatial resolution close to 18.5 km × 18.5 km (3 × 3) pixels of the Level-1 grid for each orbit. Fig. 18a shows the wind direction on December 18, 2006 in Australia. The wind direction is the azimuth angle (measured clockwise from north) that the wind is blowing from [52]. It was always great than 180° at latitudes 15°S–35°S. That means that the wind was blowing from the northeast. The wind speed (Fig. 18b) was greater than 2 m/s in that area. It was not difficult to understand that the smoke appeared to be in a more eastern position relative to the smoky pollution clouds. We concluded that the proposed algorithms well identified smoky pollution clouds. In this particular scene, we found that the distribution of the smoky pollution clouds was consistent with that of the smoke aerosol when the effects of the wind direction and speed were considered. We can conclude that the proposed algorithms can well identify smoky pollution clouds.

4. Conclusions

This study aimed to detect smoke and smoky pollution clouds based on polarized images. Our results presented that the R_p of the smoke increased with the AOD at wavelengths of 0.490 µm, 0.670 µm and 0.865 µm. However, the desert dust (DD), rural, urban and oceanic aerosols showed the opposite trend. In other words, the R_p of the aerosols decreased with the increased AOD. As a result, based on the upper polarization characteristics of the different aerosol types in three single channels, the polarized reflectance ratio was an effective means to identify smoke. The simulations and the real data measured by the PARASOL showed that the R_1, R_2 and R_3 were in the ranges of 0.3–1.0, 0.2–1.2 and 0.4–1.5, respectively.

The analysis of the R_p for pure clouds and smoky pollution clouds showed that three features could be used to identify smoky pollution clouds. First, a strong positive reflectance gradient was in the visible to near infrared spectrum. Second, a negative slope of the R_p was in a scattering angle range from 80° to 120°. In addition, compared to pure clouds, the R_p of the smoky pollution clouds was greater than 0.02 at a scattering angle ranging from 80° to 120°.

Using multidirectional, multispectral, polarized data to identify pollution cloud has two advantages: (1) It is much easier to detect smoke, because polarized light is sensitive to scattering by small particles. It is also easier to find smoky pollution clouds features in the scattering angle range from 80° to 120° with the R_p than by the total radiance. (2) Since the surface contribution to the polarized radiance was very small, the disruption can be minimized in the recognition process.

The proposed algorithms were applied in two smoke-affect regions, Australia and China, to demonstrate the effectiveness of the proposed algorithm. The detected results were also valid based on the MODIS and CALIPSO observations. The results showed that the proposed algorithm worked well in the given areas with negligible errors. This innovative technique provides a better understanding the properties of smoke and smoky pollution clouds. Moreover, it opens prospects for the use of the next-generation instrument-Chinese GF-5 DPC (directional polarimetric camera).

Acknowledgments

This work was supported by the National Natural Science Foundation of China [grant numbers 41671352]. The authors would like to thank CNES and NASA for providing the POLDER and CALIOP data used in this study. We are very grateful to the ICARE Data and Services Center for providing access to the data and for the general assistance and development support.

References

[1] Li Z, Khananian A, Fraser RH, Cihlar J. Automatic detection of fire smoke using artificial neural networks and threshold approaches applied to AVHRR imagery. IEEE Trans Geosci Remote Sens 2001;39:1859–70. doi:10.1109/36.951076.
[2] Haywood JM, Osborne SR, Francis PN, Keil A, Formenti P, Andreae MO, et al. The mean physical and optical properties of regional haze dominated by biomass burning aerosol measured from the C-130 aircraft during SAFARI 2000. J Geophys Res Atmos 2003:108 n/a-n/a. doi:10.1029/2002JD002226.
[3] Pausata FSR, Gaetani M, Messori G, Kloster S, Dentener FJ. The role of aerosol in altering North Atlantic atmospheric circulation in winter and its impact on air quality. Atmos Chem Phys 2015;15:1725–43. doi:10.5194/acp-15-1725-2015.
[4] Twomey S. The influence of pollution on the shortwave albedo of clouds. J Atmos Sci 1977;34:1149–52. doi:10.1175/1520-0469(1977)034.<1149:TIOPOT>2.0.CO;2.
[5] Albrecht BA. Aerosols, cloud microphysics, and fractional cloudiness. Science (80-) 1989;245:1227–30. doi:10.1126/science.245.4923.1227.

[6] Kaufman YJ, Koren I, Remer LA, Rosenfeld D, Rudich Y. The effect of smoke, dust, and pollution aerosol on shallow cloud development over the Atlantic Ocean. Proc Natl Acad Sci 2005;102:11207–12. doi:10.1073/pnas.0505191102.
[7] Andreae MO, Rosenfeld D, Artaxo P, Costa AA, Frank GP, Longo KM, et al. Smoking rain clouds over the Amazon. Science (80-) 2004;303:1337–42. doi:10.1126/science.1092779.
[8] Tanré D, Bräon FM, Deuzä JL, Dubovik O, Ducos F, Franäois P, et al. Remote sensing of aerosols by using polarized, directional and spectral measurements within the A-Train: the PARASOL mission. Atmos Meas Tech 2011;4:1383–95. doi:10.5194/amt-4-1383-2011.
[9] Herman M, Deuzé JL, Marchand A, Roger B, Lallart P. Aerosol remote sensing from POLDER/ADEOS over the ocean: improved retrieval using a nonspherical particle model. J Geophys Res D Atmos 2005;110:1–11. doi:10.1029/2004JD004798.
[10] Goloub P, Deuzé JL, Herman M, Fouquart Y. Analysis of the POLDER polarization measurements performed over cloud covers. IEEE Trans Geosci Remote Sens 1994;32:78–88. doi:10.1109/36.285191.
[11] Chepfer H, Goloub P, Riedi J, De Haan JF, Hovenier JW, Flamant PH. Ice crystal shapes in cirrus clouds derived from POLDER/ADEOS-1. J Geophys Res Atmos 2001;106:7955–66. doi:10.1029/2000JD900285.
[12] Costantino L, Bréon FM. Analysis of aerosol - cloud interaction from multi - sensor satellite observations. Geophys Res Lett 2010;37:1–5. doi:10.1029/2009GL041828.
[13] Xie Y, Qu JJ, Xiong X, Hao X, Che N, Sommers W. Smoke plume detection in the eastern United States using MODIS. Int J Remote Sens 2007;28:2367–74. doi:10.1080/01431160701236795.
[14] Xie Y. Detection of smoke and dust aerosols using multi-sensor satellite remote sensing measurements 2009:136.
[15] Li X, Song W, Lian L, Wei X. Forest fire smoke detection using back-propagation neural network based on MODIS data. Remote Sens 2015;7:4473–98. doi:10.3390/rs70404473.
[16] Zender CS, Krolewski AG, Tosca MG, Randerson JT. Tropical biomass burning smoke plume size, shape, reflectance, and age based on 2001-2009 MISR imagery of Borneo. Atmos Chem Phys 2012;12:3437–54. doi:10.5194/acp-12-3437-2012.
[17] Stachlewska IS, Samson M, Zawadzka O, Harenda KM, Janicka L, Poczta P, et al. Modification of local urban aerosol properties by long-range transport of biomass burning aerosol. Remote Sens 2018;10:412.
[18] Kahn RA, Gaitley BJ. An analysis of global aerosol type as retrieved by MISR. J Geophys Res Atmos 2015;120:4248–81. doi:10.1002/2015JD023322.Received.
[19] Deuzé JL, Herman M, Goloub P, Tanré D, Marchand A. Characterization of aerosols over ocean from POLDER/ADEOS-1. Geophys Res Lett 1999;26:1421–4. doi:10.1029/1999GL900168.
[20] Tanré D, Bréon FM, Deuzé JL, Herman M, Goloub P, Nadal F, et al. Global observation of anthropogenic aerosols from satellite. Geophys Res Lett 2001;28:4555–8. doi:10.1029/2001GL013036.
[21] Goloub P, Arino O. Verification of the consistency of POLDER aerosol index over land with ATSR-2/ERS-2 fire product. Geophys Res Lett 2000;27:899–902. doi:10.1029/1999GL010911.
[22] Arino O, Rosaz JM, Goloub P. The ATSR World Fire Atlas- A synergy with'Polder' aerosol products. Earth Obs Q 1999;64:1–6.
[23] Xue-hua F, Hong-bin C, Xue-hua FAN, Hong-bin C. Aerosol type identification using PARASOL multichannel polarized data aerosol type identification using PARASOL multichannel polarized data. Atmos Ocean Sci Lett 2014;7:224–9. doi:10.3878/j.issn.1674-2834.13.0088.
[24] Martins JA, Silva Dias MAF. The impact of smoke from forest fires on the spectral dispersion of cloud droplet size distributions in the Amazonian region. Environ Res Lett 2009;4:15002. doi:10.1088/1748-9326/4/1/015002.
[25] Zamora LM, Kahn RA, Cubison MJ, Diskin GS, Jimenez JL, Kondo Y, et al. Aircraft-measured indirect cloud effects from biomass burning smoke in the arctic and subarctic. Atmos Chem Phys 2016;16:715–38. doi:10.5194/acp-16-715-2016.
[26] Kaufman YJ, Nakajima T. Effect of Amazon smoke on cloud microphysics and albedo - analysis from satellite imagery. J Appl Meteorol 1993;32:729–44. doi:10.1175/1520-0450(1993)032. <0729:EOASOC>2.0.CO;2.
[27] Ackerman a S. Reduction of tropical cloudiness by soot. Science (80-) 2000;288:1042–7. doi:10.1126/science.288.5468.1042.
[28] Gautam R, Hsu NC, Kafatos M, Tsay SC. Influences of winter haze on fog/low cloud over the Indo-Gangetic plains. J Geophys Res Atmos 2007;112. doi:10.1029/2005JD007036.
[29] Gautam R, Gatebe CK, Singh MK, Várnai T, Poudyal R. Radiative characteristics of clouds embedded in smoke derived from airborne multiangular measurements. J Geophys Res 2016;121:9140–52. doi:10.1002/2016JD025309.
[30] Arakawa H. Investigation of ship tracks in ATSR-2 satellite imagery. Www-AtmPhysicsOxAcUk 2007:1–13.
[31] Lure FYM, Rau Y-C. Detection of Ship Tracks in AVHRR Cloud Imagery with Neural Networks. In: Proc. IGARSS '94 - 1994 IEEE Int. Geosci. Remote Sens. Symp., 3. IEEE; 1994. p. 1401–3. doi:10.1109/IGARSS.1994.399451.
[32] Weiss JM, Luo R, Welch RM. Automatic detection of ship tracks in satellite imagery. In: Geosci. Remote Sensing, 1997. IGARSS'97. Remote Sensing-A Sci. Vis. Sustain. Dev. 1997 IEEE Int., 1. IEEE; 1997. p. 160–2.
[33] Jiang JH, Su H, Massie ST, Schoeberl MR, Livesey NJ. A global climatology of clean and polluted clouds. AGU Fall Meet Abstr 2007.
[34] Jiang JH, Su H, Schoeberl MR, Massie ST, Colarco P, Platnick S, et al. Clean and polluted clouds: relationships among pollution, ice clouds, and precipitation in South America. Geophys Res Lett 2008;35. doi:10.1029/2008GL034631.
[35] Lee J, Kim J, Song CH, Kim SB, Chun Y, Sohn BJ, et al. Characteristics of aerosol types from AERONET sunphotometer measurements. Atmos Environ 2010;44:3110–17. doi:10.1016/j.atmosenv.2010.05.035.
[36] Kaufman YJ, Tanré D, Boucher O. A satelite view of arossols in the climate system. Nature 2002;419:215–23.
[37] Schuster GL, Dubovik O, Holben BN. Angstrom exponent and bimodal aerosol size distributions. J Geophys Res Atmos 2006:111. doi:10.1029/2005JD006328.
[38] Dubovik O, Holben BN, Kaufman YJ, Yamasoe M, Smimov A, Tanré D, et al. Single-scattering albedo of smoke retrieved from the sky radiance and solar transmittance measured from ground. J Geophys Res Atmos 1998;103:31903–23. doi:10.1029/98JD02276.
[39] Dubovik O, Holben B, Eck TF, Smirnov A, Kaufman YJ, King MD, et al. Variability of absorption and optical properties of key aerosol types observed in worldwide locations. J Atmos Sci 2002;59:590–608. doi:10.1175/1520-0469(2002)059. <0590:VOAAOP>2.0.CO;2.
[40] Hao WU, Wei Y, Gong M, Jinji MA. Research on haze aerosol particles polarization characteristics. J Atmos Environ Opt 2015;10:408–16.
[41] Smith WL, Ackerman S, Revercomb H, Huang H, DeSlover DH, Feltz W, et al. Infrared spectral absorption of nearly invisible cirrus clouds. Geophys Res Lett 1998;25:1137–40. doi:10.1029/97GL03491.
[42] Wang J, Xu X, Ding S, Zeng J, Spurr R, Liu X, et al. A numerical testbed for remote sensing of aerosols, and its demonstration for evaluating retrieval synergy from a geostationary satellite constellation of GEO-CAPE and GOES-R. J Quant Spectrosc Radiat Transf 2014;146:510–28. doi:10.1016/j.jqsrt.2014.03.020.
[43] Spurr RJD. VLIDORT: a linearized pseudo-spherical vector discrete ordinate radiative transfer code for forward model and retrieval studies in multilayer multiple scattering media. J Quant Spectrosc Radiat Transf 2006;102:316–42. doi:10.1016/j.jqsrt.2006.05.005.
[44] Li Z, Goloub P, Devaux C, Gu X, Qiao Y, Zhao F, et al. Aerosol polarized phase function and single-scattering albedo retrieved from ground-based measurements. Atmos Res 2004;71:233–41. doi:10.1016/j.atmosres.2004.06.001.
[45] Breon FM, Tanre D, Lecomte P, Herman M. Polarized reflectance of bare soils and vegetation: measurements and models. IEEE Trans Geosci Remote Sens 1995;33:487–99. doi:10.1109/36.377949.
[46] Deuzé JL, Bréon FM, Devaux C, Goloub P, Herman M, Lafrance B, et al. Remote sensing of aerosols over land surfaces from POLDER-ADEOS – 1 polarized measurements. J Geophys Res 2001;106:4913–26. doi:10.1029/2000JD900364.
[47] Winker DM, Vaughan MA, Omar A, Hu Y, Powell KA, Liu Z, et al. Overview of the CALIPSO mission and CALIOP data processing algorithms. J Atmos Ocean Technol 2009;26:2310–23. doi:10.1175/2009JTECHA1281.1.
[48] Winker DM, Pelon JR, McCormick MP. The CALIPSO mission: spaceborne lidar for observation of aerosols and clouds. In: Lidar Remote Sens. Ind. Environ. Monit. III, vol. 4893, international society for optics and photonics; 2003. p. 1. doi:10.1117/12.466539.
[49] Bréon F-M, Colzy S. Cloud detection from the spaceborne POLDER instrument and validation against surface synoptic observations. J Appl Meteorol 1999;38:777–85. doi:10.1175/1520-0450(1999)038. <0777:CDFTSP>2.0.CO;2.
[50] Li C, Ma J, Yang P, Li Z. Detection of cloud cover using dynamic thresholds and radiative transfer models from the polarization satellite image. J Quant Spectrosc Radiat Transf 2018. doi:10.1016/J.JQSRT.2018.10.026.
[51] Omar AH, Winker DM, Kittaka C, Vaughan MA, Liu Z, Hu Y, et al. The CALIPSO automated aerosol classification and lidar ratio selection algorithm. J Atmos Ocean Technol 2009;26:1994–2014. doi:10.1175/2009JTECHA1231.1.
[52] Henry RC, Chang YS, Spiegelman CH. Locating nearby sources of air pollution by nonparametric regression of atmospheric concentrations on wind direction. Atmos Environ 2002;36:2237–44. doi:10.1016/S1352-2310(02)00164-4.